

**Remarkable Strontium *B*-Site Occupancy in Ferroelectric $\text{Pb}(\text{Zr}_{1-x}\text{Ti}_x)\text{O}_3$
Solid Solutions Doped with Cryolite-Type Strontium Niobate**

Adalbert Feltz, Patrick Schmidt-Winkel,* and Michael Schossmann

EPCOS OHG

Ceramic Components Division

Corporate Research & Development

8530 Deutschlandsberg, AUSTRIA

Corwin H. Booth

Chemical Sciences Division

Lawrence Berkeley National Laboratory

Berkeley, CA 94720, USA

Jörg Albering

Institute for Chemical Technology of Inorganic Materials

Technical University

8010 Graz, AUSTRIA

* Author to whom correspondence should be addressed.

e-mail: patrick.schmidt-winkel@epcos.com

“Remarkable Strontium *B*-Site Occupancy in Ferroelectric $\text{Pb}(\text{Zr}_{1-x}\text{Ti}_x)\text{O}_3$ Solid Solutions Doped with Cryolite-Type Strontium Niobate”

April 26, 2007

Abstract

New high-performance ferroelectric materials based on $\text{Pb}(\text{Zr}_{1-x}\text{Ti}_x)\text{O}_3$ (*PZT*) that are doped with cryolite-type strontium niobate (*SNO*, $\text{Sr}_4(\text{Sr}_{2-2y/3}\text{Nb}_{2+2y/3})\text{O}_{11+y}\text{V}_{0,1-y}$ with $0 \leq y \leq 1$), hence denoted *PZT:SNO*, and their microscopic structure are described. The combination of exceptional piezoelectric properties, i.e. a piezoelectric strain constant of $d_{33} \approx 760$ pm/V, with excellent stability and degradation resistance makes ferroelectric *PZT:SNO* solid solutions very attractive for use in novel and innovative piezoelectric actuator and transducer applications. Extended X-ray absorption fine-structure (EXAFS) analyses of *PZT:SNO* samples revealed that ~10 % of the Sr cations occupy the nominal *B*-sites of the perovskite-type *PZT* host lattice. This result was supported by EXAFS analyses of both a canonical SrTiO_3 perovskite and two *SNO* model and reference compounds. Fit models that do not account for Sr cations on *B*-sites were ruled out. A clear Sr-Pb peak in Fourier transformed EXAFS data visually confirmed this structural model. The generation of temporary oxygen vacancies and the intricate defect chemistry induced by *SNO*-doping of *PZT* are crucial for the exceptional materials properties exhibited by *PZT:SNO* materials.

I. Introduction

Ferroelectric ceramic perovskites with ABO_3 -type structure such as lead zirconium titanium oxide $\text{Pb}(\text{Zr,Ti})\text{O}_3$ and its solid solutions represent the most widely used class of materials in piezoelectric actuators and transducers for their piezoelectric and dielectric properties.^{1,2} Among this class of materials, $\text{Pb}(\text{Zr}_{1-x}\text{Ti}_x)\text{O}_3$ (*PZT*) solid solutions have attracted great attention. They are ferroelectric over a wide composition range and exhibit a high Curie temperature.¹ The phase diagram of $\text{Pb}(\text{Zr}_{1-x}\text{Ti}_x)\text{O}_3$ is characterized by an unusual, nearly temperature independent morphotropic phase boundary (MPB) around $x \approx 0.45-0.50$ that separates regions with rhombohedral and tetragonal ferroelectric crystal structure.¹ In addition, $\text{Pb}(\text{Zr}_{1-x}\text{Ti}_x)\text{O}_3$ with $x \approx 0.45-0.50$ features a monoclinic bridging phase between tetragonal and rhombohedral regions.³ As a result, $\text{Pb}(\text{Zr}_{1-x}\text{Ti}_x)\text{O}_3$ solid solutions with compositions near the MPB exhibit unusually large piezoelectric coefficients and electromechanical responses.^{1,2,4,5}

The piezoelectric properties of *PZT* can change favorably in response to solid solution formation with certain compounds or doping agents, offering the possibility to tailor its properties for new applications.^{1,2} In conjunction with relatively low production costs, the unique piezoelectric, electromechanical, and dielectric properties make *PZT* and its solid solutions the material of choice for many commercial and industrial piezoelectric applications.^{2,5-7} Recently, innovative piezoelectric multilayer actuator-based diesel and gasoline injection systems were developed by major automotive suppliers (i.e. Bosch, Denso, Delphi, SiemensVDO, Toyota, etc.); and in the meantime they have already found widespread application in automotive industry.^{5,8-11} Owing to the fast electromechanical response time and the high blocking force of *PZT*-based piezoelectric multilayer actuators used in these innovative applications, the fuel injection valves can be operated at least four times faster compared to conventional solenoid-based fuel injection systems, thus enabling at least five separate fuel

“Remarkable Strontium *B*-Site Occupancy in Ferroelectric Pb(Zr_{1-x}Ti_x)O₃ Solid Solutions Doped with Cryolite-Type Strontium Niobate”

April 26, 2007

injections during one fuel injection cycle.^{5,8-11} Improved fuel economy, reduced exhaust and noise emissions, and enhanced engine performance are striking benefits directly associated with this new piezoelectric actuator-based fuel injection technology.

Aside from plain product performance, aspects like product quality and reliability as well as temporal and thermal stability are fundamentally important for high-performance electronic products. Special ferroelectric solid solution materials have therefore been developed and prepared from Pb(Zr_{1-x}Ti_x)O₃ ($x \approx 0.45-0.50$) with specific doping agents so as to optimize performance, reliability, degradation stability, and quality of piezoelectric ceramics for use in piezoelectric actuator applications.¹²⁻²²

As part of our continuing program to develop new high-performance ferroelectric materials, we recently developed and described novel perovskite-type Pb(Zr_{1-x}Ti_x)O₃ solid solutions that are doped with cryolite-type strontium niobate (*SNO*) according to the general formula $SNO = Sr_4(Sr_{2-2y/3}Nb_{2+2y/3})O_{11+y}V_{O,1-y}$ ($0 \leq y \leq 1$; V_O : oxygen vacancy).^{23,24} *SNO*-doped *PZT* materials, denoted *PZT:SNO*, exhibit exceptional piezoelectric properties and have been used successfully to manufacture high-performance piezoelectric multilayer actuators. Owing to their large piezoelectric strain constant of $d_{33} \approx 760$ pm/V (measured at an electric field of $E = 2$ kV/mm), respective piezoelectric multilayer actuators exhibit unusually large electromechanical strains of $S \approx 0.15-0.16$ %, where $S = \Delta L/L$ and L represents the length of the multilayer actuator. The unique combination of a high piezoelectric strain constant with the excellent materials stability and the high Curie temperature is caused by doping of *PZT* with cryolite-type *SNO* and by microstructure optimization in *PZT:SNO* materials.^{23,24}

We performed extended X-ray absorption fine-structure (EXAFS) analyses to gain a better microscopic understanding of these new piezoelectric *PZT:SNO* solid solutions,

“Remarkable Strontium *B*-Site Occupancy in Ferroelectric $\text{Pb}(\text{Zr}_{1-x}\text{Ti}_x)\text{O}_3$ Solid Solutions Doped with Cryolite-Type Strontium Niobate”

April 26, 2007

particularly targeting the strontium ion (Sr^{2+}) coordination environment and crystal lattice site occupancy in ferroelectric perovskite-type *PZT:SNO* materials as well as in SrTiO_3 and different *SNO* model and reference compounds.

In this paper, we report and discuss the results of our EXAFS analysis of *PZT:SNO* high-performance piezoelectric materials. In addition, we discuss their underlying intricate defect chemistry that is central to their exceptional materials properties.

II. Experimental Section

Preparation of Ceramic Samples: The ceramic samples were prepared by mixed-oxide synthesis routes. Sample preparation was carried out by wet-chemical mixing of appropriate amounts of commercially available, high-quality raw materials such as Pb_3O_4 , ZrO_2 , TiO_2 , SrCO_3 , and Nb_2O_5 with sufficiently small grain size ($d_{50} \leq 1 \mu\text{m}$). After sample isolation and drying, the corresponding powder mixtures were calcined in air, followed by wet-chemical ball-mill treatment with ZrO_2 grinding media to yield a grain size of $d_{50} \approx 0.4\text{--}0.5 \mu\text{m}$. Wet-chemical sample treatment in alcohol turned out to be advantageous. The dried powder samples were then converted into pressed-pellet samples and sintered in air to afford sintered-pellet samples with a relative density of $\rho_{\text{rel}} \sim 95\%$.

SrTiO₃ Model Compounds: Samples of the perovskite-type model compound SrTiO_3 (*STO*) were prepared from SrCO_3 and TiO_2 . After calcination at 1150°C for 6 h and subsequent fine-milling, the pressed-pellet samples were sintered at 1250°C for 4 h.

SNO Dopants and Model Compounds: Samples of cryolite-type strontium niobate $\text{Sr}_4(\text{Sr}_{5/3}\text{Nb}_{7/3})\text{O}_{11.5}\text{V}_{\text{O};0.5}$ (*SNO-1*; V_{O} : oxygen vacancy) and $\text{Sr}_4(\text{Sr}_{4/3}\text{Nb}_{8/3})\text{O}_{12}$ (*SNO-2*) were prepared analogously from SrCO_3 and Nb_2O_5 . To promote the formation of their more complicated cryolite-type structure, the *SNO* samples were subjected to a two-fold calcination treatment. The first calcination at 1100°C for 4 h was followed by ball-mill treatment for about 0.5 h. The isolated and dried powder mixtures were then subjected to a second calcination treatment at 1250°C for 4 h, followed by a second ball-mill treatment. Respective pressed-pellet samples were sintered in air at 1400°C for 4 h.

Ferroelectric PZT:SNO Ceramics:

a. Precursor Mixed-Oxide Route: *PZT:SNO* solid solution samples (*PZT* doped with cryolite-type strontium niobate, *SNO*) were prepared with a small excess of PbO as sintering aid material,

“Remarkable Strontium B-Site Occupancy in Ferroelectric Pb(Zr_{1-x}Ti_x)O₃ Solid Solutions Doped with Cryolite-Type Strontium Niobate”

April 26, 2007

for example with a composition according to formula $PZT:SNO-1 = (PZT)_{0.995}(SNO-I)_{0.005}(PbO)_{0.01}$. Pb(Zr_{0.52-0.53}Ti_{0.48-0.47})O₃ (*PZT*) and cryolite-type doping agent *SNO* were prepared separately by mixing appropriate amounts of raw materials Pb₃O₄, ZrO₂, and TiO₂ for *PZT*, and SrCO₃ and Nb₂O₅ for *SNO-1* and *SNO-2*. The *PZT* precursor powder was calcined in air at 925 °C for 6 h, and the *SNO* precursor powders were calcined twice as described above. After calcination, the *PZT* and *SNO* precursor powders were thoroughly mixed, followed by ball-mill treatment and subsequent formation of pressed-pellet samples. Sintering in air at 1100 °C for 4 h afforded sintered-pellet samples of *PZT:SNO* with a relative density of $\rho_{rel} \approx 95\%$.

b. Conventional Mixed-Oxide Route: Alternatively, *PZT:SNO* samples were prepared by mixing appropriate amounts of raw materials Pb₃O₄, ZrO₂, TiO₂, SrCO₃, and Nb₂O₅. After thorough mixing of the raw materials, ball-milling, calcination in air at 925 °C for 6 h, ball-milling, and sintering in air at 1100 °C for 4 h, sintered-pellet samples of *PZT:SNO* prepared by this synthesis route exhibited indistinguishable XRD patterns and materials properties when compared to respective *PZT:SNO* samples prepared by the *Precursor Mixed-Oxide Route*.

Particle Size Analysis: Average grain sizes and grain size distributions of powder samples were measured by light scattering of diluted aqueous or alcoholic dispersions using a MALVERN 2000 Mastersizer.

Sample Density Measurements: The experimental sample density (ρ_{exp}) of sintered-pellet samples was determined (i) by precision weighing and measuring of geometric dimensions of 10 sintered pellets per sample, and (ii) by the *Archimedes* method. The results of both experimental density determination methods were very similar. The theoretical sample density (ρ_{theo}) was derived from X-ray diffraction (XRD) analysis. The relative sample density (ρ_{rel}) was calculated according to $\rho_{rel} = \rho_{exp} / \rho_{theo}$.

X-Ray Diffraction (XRD) Analysis: Powderized sintered-pellets of samples *SNO-1*, *SNO-2*, *STO*, and *PZT:SNO* were characterized by X-ray diffraction (XRD) analysis using a Bruker AXS (Karlsruhe, Germany) D5005 θ/θ diffractometer with $\text{Cu-K}\alpha$ radiation. The diffractometer was equipped with an automatic divergence slit system, a rotating sample holder (30 rpm), a secondary graphite monochromator, and a scintillation counter. The samples were analyzed in the range of $2\theta=20\text{--}60^\circ$ (*STO* samples) and $2\theta=5\text{--}130^\circ$ (*PZT*, *PZT:SNO*, and *SNO* samples) using a step width of 0.02° and a constant counting time of 10 sec per step. Refinement of lattice constants and crystal structure according to the Rietveld profile fitting method was performed with the *TOPAS* software package (Bruker AXS, Karlsruhe, Germany). During Rietveld analysis, sample displacement and six background parameters, fitted using a polynomial of 6th degree, were refined as general parameters. For each crystal phase, the scale factor and lattice constants, the pseudo-*Voigt* peak profile coefficients, the atomic parameters, and the occupancy and thermal parameters were calculated in subsequent refinement cycles.

Extended X-ray absorption fine-structure (EXAFS) Analysis: Sintered pressed-pellet samples were ground under acetone, passed through a $32\ \mu\text{m}$ sieve, brushed onto adhesive tape, and stacked such that the change in the absorption corresponded to about half of an absorption length at the Sr *K*-edge (16105 eV) for *SNO-1*, *SNO-2*, *STO*; considerably less for *PZT:SNO*. EXAFS measurements were performed on beamline *10-2* at the Stanford Synchrotron Radiation Laboratory (*SSRL*) after loading the samples in a liquid He flow-cryostat and positioning the samples at an angle of 50° with respect to the X-ray beam. All EXAFS data were collected both in transmission and fluorescence mode with a 30-element Ge fluorescence detector, although only the fluorescence data were usable for *PZT:SNO*. Data were acquired at the Sr *K*-edge in the temperature range of 20-300 K. The Si (220) monochromator was detuned by 75 % to reduce harmonic contamination. High quality EXAFS data were obtained for all samples. Typically

April 26, 2007

two to three scans were performed on samples of model compounds *STO*, *SNO-1* and *SNO-2*, but 17 scans were run on *PZT:SNO* samples over the course of about 7.5 hours.

The EXAFS function $\chi(k)$ describes the normalized oscillations measured above a given absorption edge.²⁵ The photoelectron wave vector k is determined by $k = \sqrt{(8\pi^2 m_e / h^2)(E - E_0)^2}$, where m_e is the electron rest mass and E is the photon incident energy. E_0 is the photoelectron threshold energy, arbitrarily determined from the energy position of the half-height of the given absorption edge. The outgoing photoelectron can be backscattered by neighboring atoms and can therefore interfere with itself in the vicinity of the absorbing atom. This interference modulates the absorption coefficient in a manner proportional to the number of generated photoelectrons. χ is therefore defined as $\chi = \mu_a / \mu_0 - 1$, where μ_a is the absorption from the atomic species of interest and μ_0 is an approximation of this absorption in the absence of EXAFS oscillations. In fluorescence mode EXAFS measurements, the true χ is approximated by $\chi_{\text{exp}} = I_f / I_0 - 1$, where I_f is the measured fluorescence flux and I_0 is the incident flux. As these data are subject to self-absorption of the fluorescence photons, we made a correction for this effect to obtain an approximation to the true χ .²⁶ Given the high quality of the transmission data on *STO* samples, we were able to verify the accuracy of the self-absorption correction on the fluorescence data. Although the correction was quite large (20-30 %) in the model compounds, the correction was only about 1 % in case of *PZT:SNO* samples where only the fluorescence data is usable. The data were also corrected for the dead time of the Ge detector. All recorded EXAFS data were reduced and fit in real space using the *RSXAP* programs,²⁷⁻²⁹ utilizing theoretical photoelectron backscattering amplitudes and phases generated by the *FEFF7* code.³⁰ In particular, μ_0 was approximated by a 7-knot cubic spline.

III. Results and Discussion

X-Ray Diffraction (XRD) Analysis: The results of our X-ray crystallography and XRD analysis of *STO* samples confirmed the well known perovskite-type structure of SrTiO_3 with $a=3.90489(1)$ Å. In the ideal perovskite ABO_3 lattice with a cubic unit cell as shown in Figure 1, Sr^{2+} ions on *A*-sites are surrounded by the faces of $[\text{TiO}_{6/2}]^{2-}$ octahedra. Sr^{2+} ions on *A*-sites therefore possess 12 immediate oxygen neighbors, so-called Sr(*A*)-O neighbors, at a distance of $R\approx 2.76$ Å.

Figure 2 shows a representative XRD pattern of $PZT:SNO-I = [(\text{PZT})_{0.995}(\text{SNO}-I)_{0.005}(\text{PbO})_{0.01}]$. The unit cell is closely related to the ideal perovskite structure shown in Figure 1. However, the structure of $PZT:SNO-I$ is modified from the ideal ABO_3 structure by ferroelectric tetragonal and rhombohedral distortions that result from the specific Zr^{4+} -to- Ti^{4+} ratio in PZT near the morphotropic phase boundary (MPB), that is for $x\approx 0.45$ - 0.50 in $\text{Pb}(\text{Zr}_{1-x}\text{Ti}_x)\text{O}_3$.¹ In our case, parameter x was fixed to $0.47\leq x\leq 0.48$. The XRD patterns show no indications for secondary phases such as PbO or $\text{Pb}_2\text{Nb}_2\text{O}_7$ (pyrochlore). The individual contributions and fractions of respective co-existing ferroelectric tetragonally and rhombohedrally distorted phases in $PZT:SNO$ near the MPB were determined by Rietveld refinement calculations. For $PZT:SNO-I$, the fractional contribution of the tetragonal phase is 48.9 mass-% with lattice constants of $a=4.0440(7)$ Å and $c=4.1238(8)$ Å, while the fraction of the rhombohedral phase is 51.1 mass-% with lattice constants of $a=5.768(6)$ Å and $c=7.06(1)$ Å. These values are controlled by parameter x according to general formula $\text{Pb}(\text{Zr}_{1-x}\text{Ti}_x)\text{O}_3$.¹ As expected, the small excess of about 1 mol-% of PbO that was added as sintering aid material, and the low concentration (≈ 0.5 mol-%) of cryolite-type dopant $\text{SNO}-I = \text{Sr}_4(\text{Sr}_{5/3}\text{Nb}_{7/3})\text{O}_{11.5}\text{V}_{0.5}$, which forms a solid solution with the PZT host lattice, could not be detected by XRD analysis.

The cryolite-type structure of dopant *SNO-I*, illustrated schematically in Figure 3a, is closely related to the perovskite-type *ABO*₃ structure (Figure 1). This relation becomes readily apparent by comparison with Figure 3b, which shows a portion of the upper right region of the unit cell displayed in Figure 3a. With the co-existence of both Sr²⁺ and Nb⁵⁺ ions, octahedral *B*-sites in the cryolite-type structure of *SNO-I* (Figure 3a) are predominantly occupied by Sr²⁺ and Nb⁵⁺ ions in alternating sequence. This leads to a doubling of the lattice parameter, and therefore an enlarged unit cell containing two formula units of *SNO-I* according to Sr₈(Sr_{10/3}Nb_{14/3})O₂₃V_{O;1} = 2 × Sr₄(Sr_{5/3}Nb_{7/3})O_{11.5}V_{O;0.5} is obtained. Based on the face-centered cubic (fcc) packing of [SrO₃]⁴⁻ units, the [NbO_{6/2}]⁻ octahedra are slightly contracted owing to higher charged Nb⁵⁺ ions ($r_{\text{Nb}(5+), \text{CN}=6} = 0.64 \text{ \AA}$). The contraction of the [NbO_{6/2}]⁻ octahedra makes it possible for larger Sr²⁺ ions ($r_{\text{Sr}(2+), \text{CN}=6} = 1.18 \text{ \AA}$) to occupy the center position (*B*-site) of adjacent [SrO_{6/2}]⁴⁻ octahedra (Figure 3a).

A representative XRD pattern of cryolite-type dopant Sr₄(Sr_{5/3}Nb_{7/3})O_{11.5}V_{O;0.5} (*SNO-I*) is depicted in Figure 4. Rietveld refinement confirmed the cryolite-type structure of *SNO-I*. The space group *Fm*3*m* with $a = 8.29833(3) \text{ \AA}$ was determined, not only based on the assumption of ideal crystallographic positions in the cryolite-type structure for *SNO-I*, but also when split positions (i) of Sr²⁺ and (ii) of Sr²⁺ and O^{-II} were used for Rietveld refinement. The XRD data are in good agreement with previous studies^{31,32} of the SrO-Nb₂O₅ phase diagram that revealed the existence of a non-stoichiometric region corresponding to general *SNO* formula Sr₄(Sr_{2-2y/3}Nb_{2+2y/3})O_{11+y}V_{O;1-y} (0 ≤ y ≤ 1). While for a compound with the composition Sr₄(Sr_{1.44}Nb_{2.56})O_{11.84}V_{O;0.16} a cubic unit cell with $a = 8.277 \text{ \AA}$ was determined, XRD analysis of a material corresponding to formula Sr₄(Sr_{1.92}Nb_{2.08})O_{11.12}V_{O;0.88} resulted in a cubic unit cell with $a = 8.314 \text{ \AA}$.³¹ A strong correlation exists between the oxygen vacancy concentration [*V*_O] and the Sr²⁺-to-Nb⁵⁺ ratio (*B*_{Sr}/*B*_{Nb}) on the octahedral *B*-sites in the material's crystal lattice.³¹

For the first boundary case with a material composition corresponding to formula Sr₄(Sr₂Nb₂)O₁₁V_{O;1} ($B_{\text{Sr}}/B_{\text{Nb}}=1$ and $y=0$), a tetragonal lattice distortion with $a=8.417$ Å and $c=16.41$ Å was determined by XRD analysis and Rietveld refinement.³¹ In this case, the enlarged unit cell comprised four formula units corresponding to Sr₁₆(Sr₈Nb₈)O₄₄V_{O;4} = 4 × Sr₄(Sr₂Nb₂)O₁₁V_{O;1}, which includes four oxygen vacancies V_O.³¹ For the second boundary case corresponding to the oxygen vacancy-free composition Sr₄(Sr_{4/3}Nb_{8/3})O₁₂ = 4 × Sr(Sr_{1/3}Nb_{2/3})O₃ = 4/3 × Sr₄Nb₂O₉ (*SNO-2*; $B_{\text{Sr}}/B_{\text{Nb}}=1/2$ and $y=1$), our XRD analysis and Rietveld refinement gave rise to a cubic unit cell with space group *Fm3m* and lattice parameter $a=8.2671$ Å. This lattice constant is in good agreement with the cubic *F*-centered unit cell with lattice parameter $a=8.268(2)$ Å that was described previously^{33,34} for a so-called high temperature (*HT*) modification of compound Sr₄Nb₂O₉ (*HT-Sr₄Nb₂O₉*) corresponding to the cryolite-type composition Sr[(Sr_{2/3}Nb_{1/3})_{1/2}Nb_{1/2}]O₃ = 1/3 × Sr₄Nb₂O₉, featuring a 1:1 ordering of (Sr_{2/3}Nb_{1/3}):(Nb) on the nominal *B*-sites.^{33,34} XRD and neutron scattering data indicated Sr(*A*-site)-O bond lengths in the range of $R\approx 2.361$ - 3.487 Å, and a Sr(*B*-site)-O bond length of $R\approx 2.198$ Å.³⁴ After annealing *HT-Sr₄Nb₂O₉* samples at 1100-1200°C, a phase transition occurred and a low temperature (*LT*) polymorph phase (*LT-Sr₄Nb₂O₉*) was identified.³⁴ Transmission electron microscopy (TEM) analysis revealed that, in contrast to the *HT-Sr₄Nb₂O₉* phase, the *LT-Sr₄Nb₂O₉* polymorph with orthorhombic unit cell does not exhibit alternation of Nb- and Sr/Nb-occupied {111}_{*c*} cation planes.³⁴ For *LT-Sr₄Nb₂O₉*, TEM data suggested a sequence of nine {111}_{*c*} cation planes according to (Sr_{1/2}NbNbNbSrSrNbNbNbSr_{1/2}...) that is consistent with a Sr²⁺-to-Nb⁵⁺ ratio on *B*-sites of $B_{\text{Sr}}/B_{\text{Nb}}=1/2$.³⁴

Extended X-Ray Absorption Fine-Structure (EXAFS) Analysis: Representative Sr *K*-edge EXAFS data measured at a temperature of 20 K for *PZT:SNO-1* samples are shown in Figure 5 as a function of the photoelectron wave vector k . A Fourier transform of these EXAFS data produces peaks as a function of the scattering distance r (x -axis on Fourier transform) from the backscattering atoms, corresponding to scattering shells in the polycrystal (Figure 6).²⁵ However, phase shifts of the photoelectrons at both the absorbing and backscattering atoms or ions create shifts from the real bond length R for a given pair, as well as constructive and destructive interference. Therefore, careful fitting with established scattering functions was required to extract quantitative local structure information. First, fits to SrTiO_3 (*STO*) data are described that help establish the overall scale factor S_0^2 . Next, the efficacy of the fitting model for determining Sr *B*-site occupancy is tested on the *SNO* samples. Finally, the *PZT:SNO* fits are described.

Fits to the measured EXAFS data of the *STO* model compound gave results that are consistent with the expected perovskite structure. The pair-distance distribution variance σ^2 for the nearest Sr-O neighbors was fairly large and could not be explained solely by thermal vibrations, indicating a possible local lattice distortion that was not expected from X-ray crystallography. The typical overall scale factor for Sr *K*-edge EXAFS analysis is $S_0^2=1.0$;³⁵ however, the measured overall scale factor is $S_0^2=1.35$ for the present data (reproducible within ~5 %). This discrepancy is likely due to a correlation between the presence of a local lattice distortion and an enhanced overall scale factor in the fits. When the overall scale factor was fixed at $S_0^2=1.0$ in our EXAFS analysis and the resulting pair-distance distribution variance values were subsequently fit with a correlated Debye model,³⁶ we obtained the reasonable result that the Sr-O bond has a slightly enhanced non-thermal variance (i.e. static disorder) of $0.0020(7) \text{ \AA}^2$, while the eight Sr-Ti bonds at $R \approx 3.4 \text{ \AA}$ and the six Sr-Sr pairs at $R \approx 3.9 \text{ \AA}$ possess

April 26, 2007

no measurable static disorder. Such a distortion would occur for a simple local rotation of the [TiO_{6/2}]²⁻ octahedra. Note that any such distortion must necessarily not possess long-range order, since it has not been observed in diffraction experiments. More experimental EXAFS data, particularly from the Ti *K*-edge, would be required to pursue this matter further. The thermal parameters are otherwise consistent with previous measurements at the Ti *K*-edge³⁷ and are typical based on our experience with manganese perovskites.³⁸

According to previous investigations,³⁴ the *SNO* samples are expected to be substantially distorted and possess a more complex structure relative to *STO* samples. In fact, the Fourier transforms shown in Figure 6 reflect this situation. Distortions are expected not only in *SNO* samples, but also in *PZT:SNO*. These distortions and the complicated nature of two-site fits necessitate a fitting model to be developed for determining the fractional Sr *B*-site occupancy f_B , and this model has been tested on the *SNO* samples. The fitting model is based on the *STO* and Sr₄Nb₂O₉ structures,³⁴ in which the number of neighbors around each Sr²⁺ is determined by one parameter, namely f_B . Most of the bond lengths were allowed to vary unconstrained to the ideal structure and had substantially enhanced pair-distance distribution variance values of $\sigma^2 \sim 0.03 \text{ \AA}^2$. These enhanced σ^2 values indicate distortions in the *SNO* samples relative to an ideal perovskite. The main differences between the *A*-sites and the *B*-sites in this structure are the nearest-neighbor oxygen coordination and the identity of the nearest metal neighbor: The *A*-site has 12 Sr(*A*)-O pairs at a bond length $R \approx 2.94 \text{ \AA}$, followed by $8f_B$ Sr(*A*)-Sr(*B*) pairs and $8(1-f_B)$ Sr(*A*)-Nb (*B*) pairs at $R \approx 3.59 \text{ \AA}$. The *B*-site, on the other hand, features 6 Sr(*B*)-O pairs at $R \approx 2.16 \text{ \AA}$ and 8 Sr(*B*)-Sr(*A*) pairs at $R \approx 3.59 \text{ \AA}$. For example, in Sr₄Nb₂O₉, the fraction of Sr²⁺ on the *B*-site is $f_B = 0.25$, and so the *A*-site has 2 Sr(*A*)-Sr(*B*) pairs at $R \approx 3.59 \text{ \AA}$. Since the electron

April 26, 2007

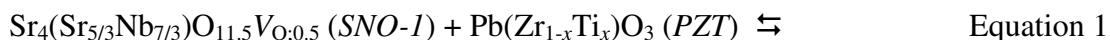
scattering amplitudes for Sr²⁺ and Nb⁵⁺ are very similar, the EXAFS data of the *SNO* samples are sensitive to the Sr *B*-site occupancy primarily through the nearest-neighbor oxygen peaks.

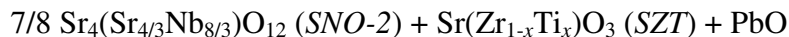
Using the above fitting model, the fraction of Sr²⁺ ions on the *B*-site was allowed to vary, but the overall scale factor was fixed to $S_0^2=1.0$ in fits to the *SNO* data. The quality of the fits is very good, considering these necessary assumptions and simplifications. For *SNO-1* and *SNO-2*, the following fractions of Sr²⁺ ions on *B*-sites are obtained by EXAFS analysis: $f_{B,\text{exp}}(\text{Sr})=32(2)$ % for Sr₄(Sr_{5/3}Nb_{7/3})O_{11.5}V_{O;0.5} (*SNO-1*) and $f_{B,\text{exp}}(\text{Sr})=33(2)$ % for Sr₄(Sr_{4/3}Nb_{8/3})O₁₂ (*SNO-2*). Nominally, $f_B(\text{Sr})=29$ % and $f_B(\text{Sr})=25$ %, respectively, would be expected for *SNO-1* and *SNO-2*. The EXAFS errors were determined using a Monte Carlo method,²⁸ and primarily reflect errors in reproducibility. Comparisons to the nominal f_B values indicate that the systematic errors may be as large as 30 %.

In contrast to the *SNO* data, the *PZT:SNO* EXAFS data is sensitive to the Sr *B*-site occupancy both in the nearest-neighbor oxygen coordination and in the near-neighbor metal scattering peaks, because the scattering amplitudes of Pb²⁺ and Ti⁴⁺ cations contrast strongly with those of Sr²⁺, Nb⁵⁺, and Zr⁴⁺ cations. In addition, while *PZT* is distorted relative to the ideal perovskite structure,³ the distortions are much simpler than in Sr₄Nb₂O₉.³⁴ The *PZT:SNO* fitting model is therefore based on the tetragonal *P4mm* structure of *PZT*,³ rather than the ideal perovskite structure. Hence many distortions, which had to be modeled with an enhanced σ^2 in the *SNO* fits, are explicitly included, as will be seen below. These advantages should make the measurement of f_B even more reliable in *PZT:SNO* samples than in *SNO* samples. Although the distortions require more scattering shells to be included in the fit, the peak separation is generally quite good considering the different species in each shell. Although the number of varied parameters is relatively large at 23, this value is far below the number of 40 independent data points given by *Stern's* rule.³⁹

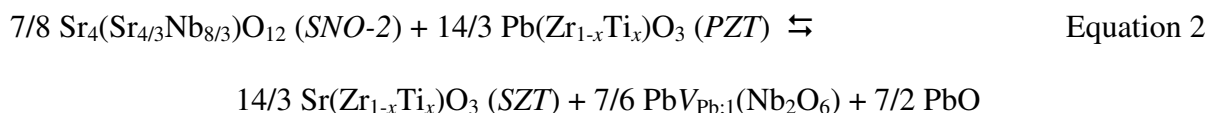
Figure 7 shows representative Sr *K*-edge EXAFS data for ceramic material *PZT:SNO-I*, together with two fits (see Table I for fit details). The measured σ^2 values (Table 1) are unusually small for the Sr(*B*)-Pb and Sr(*B*)-Ti pairs, most likely due to small differences between the real distortions and the fit model. Fits that constrain Sr²⁺ ions onto the Pb²⁺ site (*A*-site) do not reproduce the peak at $r \approx 3.3$ Å, while fits that allow 10±3 % of Sr²⁺ ions to occupy the Zr⁴⁺,Ti⁴⁺ site (*B*-site) reproduce the peak at $r \approx 3.3$ Å very well. The most prominent difference between these two fitting models is the presence of a Sr-Pb pair at $R \approx 3.42$ Å. In addition, other smaller peaks occurring at higher *r*-values are much better reproduced by the fit that allows 10±3 % of Sr²⁺ ions on the *B*-site. The measured *B*-site fraction for Sr²⁺ ions is well reproduced at all four measurement temperatures, and it is not sensitive to our choice of $S_0^2=1.0$. In addition, an *F*-test (*Hamilton test*)⁴⁰⁻⁴² considering structure models with different fractions of Sr²⁺ cations on *B*-sites, namely $f_B(\text{Sr})=10$ % versus $f_B(\text{Sr})=0$, rules out the latter with 99 % confidence. All the above mentioned findings are consistent and indicate very strongly that 10±3 % of the Sr²⁺ cations present in *PZT:SNO-I* occupy the nominal *B*-sites of the *PZT* host lattice.

Discussion of Defect Chemistry: The formal composition of solid solution *PZT:SNO-I* corresponds to $(PZT)_{0.995}(SNO-I)_{0.005}(\text{PbO})_{0.01}$ or, more specifically, $[\text{Pb}(\text{Zr}_{0.52-0.53}\text{Ti}_{0.48-0.47})\text{O}_3]_{0.995}[\text{Sr}_4(\text{Sr}_{5/3}\text{Nb}_{7/3})\text{O}_{11.5}\text{V}_{\text{O};0.5}]_{0.005}[\text{PbO}]_{0.01}$. This formula implies that ≈ 29.4 % (5/17) of Sr²⁺ cations occupy the octahedral *B*-sites in the perovskite-type *PZT* host lattice. Owing to the stronger basicity of SrO compared to PbO, the following chemical reaction between *PZT* and *SNO-I* has to be considered:





The reaction shown in Equation 1 affords (i) strontium niobate *SNO-2* that is free of oxygen vacancies, (ii) strontium zirconium titanium oxide (*SZT*), and (iii) PbO as reaction products. *SNO-2* and *SZT* are taken up by or dissolved in the *PZT* matrix. After complete chemical reaction of *SNO-1* and *PZT* according to Equation 1, only $\approx 20.6\%$ (7/34) of Sr²⁺ cations would occupy the octahedral *B*-sites in the *PZT* host lattice of the corresponding solid solution, and no oxygen vacancies would exist. In addition, the subsequent chemical reaction shown in Equation 2 would give rise to complete vanishing of Sr²⁺ ions from nominal *B*-sites, along with the formation of lead vacancies V_{Pb} on *A*-sites:



Based on the findings of our EXAFS analysis (see above), which indicated that $10 \pm 3\%$ of the Sr²⁺ ions occupy the nominal *B*-sites in *PZT:SNO-1* solid solutions, and based on the chemical reactions between *SNO-1* and *PZT* (Equation 1) as well as *SNO-2* and *PZT* (Equation 2), the following chemical composition is derived for *PZT:SNO-1* after sintering and cooling:

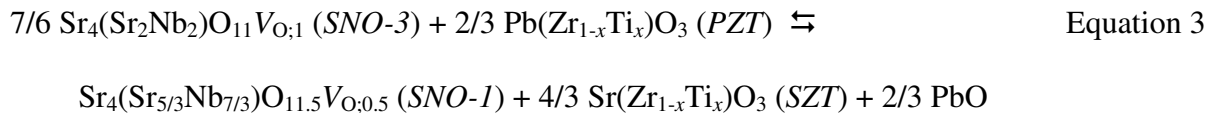


In *PZT:SNO-1*, a residual concentration of Sr²⁺ ions on the nominal *B*-sites is valence-compensated by Nb⁵⁺ ions in a typical cryolite-type configuration without the formation of oxygen vacancies. In addition, *SZT* and Pb(Nb₂O₆) that can be formed according to Equation 2

April 26, 2007

are taken up and dissolved in the perovskite-type *PZT* host lattice. The chemical reaction according to Equation 2 implies the formation of lead vacancies V_{Pb} on *A*-sites. Another beneficial result of the solid-state reactions shown in Equations 1 and 2 is the *in situ* generation of PbO that can serve as sintering aid material for *PZT:SNO*.

The generation of PbO by acid-base reaction of *PZT* and *SNO*-dopant (Equation 1) is expected to be exothermic. During sintering at high temperature, the chemical equilibrium would therefore be shifted to the left-hand side, giving rise to the formation of oxygen vacancies. As shown in Equation 3, even the *SNO* compound according to $\text{Sr}_4(\text{Sr}_2\text{Nb}_2)\text{O}_{11}\text{V}_{\text{O};1}$ (*SNO-3*), which corresponds to the extreme boundary composition of the non-stoichiometric range of the $\text{SrO-Nb}_2\text{O}_5$ phase diagram with cryolite-type structure,^{31,32} can participate in the series of important temperature-dependent equilibrium reactions and therefore promote the formation of ferroelectric *PZT:SNO* solid solutions.



It has been an essential part of our piezoelectric materials design concept to intentionally induce temporary oxygen vacancies in the *PZT* host lattice of high-performance ferroelectric *PZT*-based solid solutions during thermal processing (esp. sintering) by means of doping with cryolite-type *SNO* in order to facilitate sintering and promote optimized microstructure formation. During post-sintering cooling of *PZT:SNO*, the temporary oxygen vacancies are substantially annihilated, essentially by shifting the equilibrium reactions shown in Equations 1-3 to the right-hand side and by re-filling with oxygen. These processes and the associated intricate

“Remarkable Strontium *B*-Site Occupancy in Ferroelectric $\text{Pb}(\text{Zr}_{1-x}\text{Ti}_x)\text{O}_3$ Solid Solutions Doped with Cryolite-Type Strontium Niobate”

April 26, 2007

defect chemistry are crucial for the exceptional piezoelectric properties and the excellent stability and degradation resistance exhibited by ferroelectric *PZT:SNO* solid solutions.

IV. Summary and Conclusion

New high-performance Pb(Zr_{1-x}Ti_x)O₃ (*PZT*)-based ferroelectric solid solutions, denoted *PZT:SNO*, are described. They can be sintered at reasonably low temperatures ($T_S \leq 1100$ °C), exhibit excellent long-term stability and degradation resistance, and they give rise to exceptional piezoelectric properties. These properties are essentially achieved by controlling the material's defect chemistry, particularly by intentional generation of temporary oxygen vacancies in the *PZT* host lattice in order to facilitate sintering and promote optimized microstructure formation. Key to our material design concept are dopants based on cryolite-type strontium niobate (*SNO*) according to the general formula Sr₄(Sr_{2-2y/3}Nb_{2+2y/3})O_{11+y}V_{O,1-y} with $0 \leq y \leq 1$. The microscopic structure of ferroelectric perovskite-type *PZT:SNO* was investigated in particular by EXAFS analysis, which served as a powerful method to study the crystal lattice site occupancy of Sr²⁺ ions in *PZT:SNO* samples as well as in SrTiO₃ and *SNO* model and reference compounds. In *PZT:SNO*, Sr²⁺ ions with coordination numbers of $CN_{Sr} = 12$ (*A*-site occupancy) and $CN_{Sr} = 6$ (*B*-site occupancy) coexist. Our EXAFS analyses revealed that a remarkable portion of 10 ± 3 % of the Sr²⁺ ions occupy the nominal *B*-sites (Zr⁴⁺, Ti⁴⁺ sites) in the perovskite-type *PZT* host lattice of *PZT:SNO-1* samples. This result is supported by EXAFS analyses of both a canonical SrTiO₃ perovskite and two *SNO* compounds, namely Sr₄(Sr_{5/3}Nb_{7/3})O_{11.5}V_{O,0.5} (*SNO-1*) and Sr₄(Sr_{4/3}Nb_{8/3})O₁₂ (*SNO-2*), which served as model and reference materials. In addition, fit models that did not include Sr²⁺ ions on *B*-sites were ruled out by an *F*-test (*Hamilton* test). The clear presence of a Sr-Pb peak in the Fourier transformed EXAFS data of *PZT:SNO* samples served as further visual and qualitative confirmation of this structural model.

The generation of temporary oxygen vacancies and the intricate defect chemistry, both of which are induced and controlled by *SNO*-doping of *PZT*, are crucial for the exceptional piezoelectric properties and the excellent stability and degradation resistance exhibited by

“Remarkable Strontium *B*-Site Occupancy in Ferroelectric $\text{Pb}(\text{Zr}_{1-x}\text{Ti}_x)\text{O}_3$ Solid Solutions Doped with Cryolite-Type Strontium Niobate”

April 26, 2007

PZT:SNO solid solutions. To the best of our knowledge, the results described in this research work constitute the first published experimental verification for substantial *B*-site occupancy of Sr^{2+} ions in *PZT*-based ferroelectric solid solutions.

V. Acknowledgments and Support

A.F., P.S.W., and M.S. thank H. Florian, Dr. C. Hoffmann, and the management of EPCOS OHG and EPCOS AG for support of this research project. C.H.B. was supported, in part, by the U.S. Department of Energy (DOE) under Contract No. DE-AC02-05CH11231. Portions of this research were carried out at the Stanford Synchrotron Radiation Laboratory (SSRL), a national user facility operated by Stanford University on behalf of the U.S. DOE, Office of Basic Energy Sciences.

The piezoelectric materials studied in this research project were developed and prepared solely by EPCOS prior to this investigation. C.H.B. (LBNL) and J.A. (TU Graz) carried out EXAFS analysis and XRD analysis, respectively on piezoelectric materials as well as model and reference compounds developed, synthesized, and provided by EPCOS. Both EXAFS and XRD analyses were performed by order of and for account of EPCOS. The experimental results of both EXAFS analysis and XRD analysis confirmed and verified the original material design concept developed by EPCOS prior to this investigation.

VI. References

1. B. Jaffe, W. R. Cook, and H. Jaffe, “Piezoelectric Ceramics,” Academic Press, New York, NY, 1971.
2. G. H. Haertling, “Ferroelectric Ceramics: History and Technology,” *J. Am. Ceram. Soc.*, **82** [4] 797-818 (1999).
3. B. Noheda, J. A. Gonzalo, L. E. Cross, R. Guo, S.-E. Park, D. E. Cox, and G. Shirane, “Tetragonal-to-Monoclinic Phase Transition in a Ferroelectric Perovskite: The Structure of $\text{PbZr}_{0.52}\text{Ti}_{0.48}\text{O}_3$,” *Phys. Rev. B*, **61** [13] 8687-8695 (2000).
4. H. Fu and R. E. Cohen, “Polarization Rotation Mechanism for Ultrahigh Electromechanical Response in Single-Crystal Piezoelectrics,” *Nature*, **403**, 281-283 (2000).
5. C. A. Randall, A. Kelnberger, G. Y. Yang, R. E. Eitel, and T. R. ShROUT, “High Strain Piezoelectric Multilayer Actuators - A Materials Science and Engineering Challenge,” *J. Electroceram.*, **14**, 177-191 (2005).
6. J. Pritchard, C. R. Bowen, and F. Lowrie, “Multilayer Actuators: Review,” *Brit. Ceram. Trans.*, **100**, 265–273 (2001).
7. K. Uchino, “Recent Trend of Piezoelectric Actuator Developments,” pp. 3-9 in *Proceedings of International Symposium on Micromechatronics and Human Science*; Nagoya, Japan, Nov. 23-26, 1999; IEEE: Piscataway, NJ, 1999.
8. K. Egger, “Diesel Technology–Ceramic Muscle”, *Automotive Engineer*, **27** [1] 52-54 (2002).
9. D. Schoeppe, P. Bercher, N. Guerrassi, and P. Spadafora, “Common Rail Technology for Future Low Emission Diesel Vehicles;” pp. 1137-1155 in *Proceedings of 13th Aachen Colloquium: Vehicle- und Engine Technology*; Aachen, Germany, Oct. 4-6, 2004; Vol. 2, 2004.

10. H. Yanagihara, Y. Sato, and J. Mizuta, “A Study of DI Diesel Combustion under Uniform Higher-Dispersed Mixture Formation,” *JSAE Review*, 18 [3] 247-254 (1997).
11. D. Schoeppe, P. Bercher, N. Guerrassi, and P. Spadafora, “Evolving Diesel Common Rail Technology for Future Low Emission Standards,” pp. 31-49 in *Proceedings of Diesel- and Gasoline Direct Injection III, 4th Conference, Injection Systems: Potential, Applications, Future Developments*; Berlin, Germany, Dec. 2-3, 2004; Vol. 40. Edited by E. Steinmetz. Expert Verlag, 2004.
12. D. Cramer, H. Hellebrand, and K. Lubitz, “Process for Manufacturing Monolithic Multilayer Piezoelectric Actuator,” *US 6,230,378 B1* (2001).
13. M. Hammer and M. J. Hoffmann, “Detailed X-ray Diffraction Analyses and Correlation of Microstructural and Electromechanical Properties of La-doped *PZT* Ceramics,” *J. Electroceram.*, 2 [2] 75-84 (1998).
14. M. Hammer, M. Kühlein, and H. Böder, “Piezoelectric Ceramic Material, Method for Production Thereof, and Electroceramic Multi-Layer Component,” *US 6,773,621 B2* (2004).
15. H. Böding, K. Lubitz, and C. Schuh, “Piezoceramic Composition, Piezoceramic Body Comprising said Composition, and Method for Producing said Composition and said Body,” *US 2005258718 A1* (2005).
16. T. Kawamoto, “Piezoelectric Ceramic, Multilayered Piezoelectric Element, and Injector,” *JP 2001342062 A* (2001).
17. T. Kawamoto, “Piezoelectric Ceramic for Actuator, Layer-Built Piezoelectric Actuator and Jetting Apparatus,” *JP2002293625 A* (2002).
18. K. Horikawa and S. Kawada, “Piezoelectric Material Ceramic Composition for Piezoelectric Ceramic Electric Component, contains Lead-Titanium-Zirconium Oxide of Specific Composition,” *WO 2006038389 A1* (2006).

“Remarkable Strontium B-Site Occupancy in Ferroelectric Pb(Zr_{1-x}Ti_x)O₃ Solid Solutions Doped with Cryolite-Type Strontium Niobate”

April 26, 2007

19. S. Sasaki, “Piezoelectric Ceramic, Method of Manufacturing the Same, and Piezoelectric Device,” *US 6,979,410 B2* (2005).
20. T. Keiichi, N. Masamitsu, and K. Koichi, “Piezoelectric Element Material and its Production,” *JP 07277822 A* (1995).
21. K. Okuda, Y. Goto, S. Minami, and H. Moriwaki, “Method of Producing Piezoelectric Ceramic Device,” *US 2005115039 A1* (2005).
22. S. Henneck, G. Hejtmann, M. Kühlein, A. Kelnberger, and A. Okumus, “Method for Producing *PZT*-Based High-Performance Piezoceramics,” *WO 2006000491 A1* (2006).
23. A. Feltz, H. Florian, and M. Schossmann, “Ceramic Material,” *WO 2005069396 A1* (2005).
24. M. Schossmann, A. Feltz, and H. Florian, “Keramikmaterial,” *DE 102004002204 A1* (2005).
25. B. K. Teo, “EXAFS: Basic Principles and Data Analysis,” Springer-Verlag, New York, 1986.
26. C. H. Booth and F. Bridges, “Improved Self-Absorption Correction for Fluorescence Measurements of Extended X-Ray Absorption Fine-Structure,” *Physica Scripta* **T115**, 202 (2005).
27. T. M. Hayes and J. B. Boyce, “Extended X-Ray Absorption Fine Structure Spectroscopy;” pp. 173-351 in *Solid State Physics*, Vol. 37. Edited by H. Ehrenreich, F. Seitz, and D. Turnbull. Academic Press, New York, NY, 1982.
28. G. G. Li, F. Bridges, and C. H. Booth, “X-Ray Absorption Fine-Structure Standards: A Comparison of Experiment and Theory,” *Phys. Rev. B*, **52** [9] 6332-6348 (1995).
29. <http://lise.lbl.gov/R SXAP/>
30. S. I. Zabinsky, J. J. Rehr, A. Ankudinov, R. C. Albers, and M. J. Eller, “Multiple-Scattering Calculations of X-Ray Absorption Spectra,” *Phys. Rev. B* **52** [4] 2995-3009 (1995).

“Remarkable Strontium B-Site Occupancy in Ferroelectric Pb(Zr_{1-x}Ti_x)O₃ Solid Solutions Doped with Cryolite-Type Strontium Niobate”

April 26, 2007

31. P. P. Leshchenko, A. V. Shevchenko, L. N. Lykova; L. M. Kovba, and E. A. Ippolitova, “Systema SrO-Nb₂O₅,” *Izv. Akad. Nauk SSSR, Neorg. Mater.*, **18** [7] 1202-1205 (1982); *Inorg. Mater. (Engl. Transl.)*, **18** [7] 1013-1016 (1982).
32. Phase diagram for system SrO-Nb₂O₅, p. 4, Fig. 92-006 in *Phase Equilibria Diagrams: Phase Diagrams for Ceramists*, Annual '92. Edited by A. E. McHale. American Ceramic Society, Westerville, OH, 1992.
33. M. Hervieu, B. Raveau, J. Lecomte, and J. P. Loup, “Le Niobate de Strontium Sr₄Nb₂O₉: Une Pérovskite Complexe,” *Rev. Chim. Min.*, **22**, 44-57 (1985).
34. I. Levin, J. Y. Chan, J. H. Scott, L. Farber, T. A. Vanderah, and J. E. Maslar, “Complex Polymorphic Behavior and Dielectric Properties of Perovskite-Related Sr(Sr_{1/3}Nb_{2/3})O₃,” *J. Solid State Chem.*, **166**, 24-41 (2002).
35. P. D’Angelo, H.-F. Nolting, and N. V. Pavel, “Evidence for Multi-Electron Resonances at the Sr K-Edge,” *Phys. Rev. A*, **53** [2] 798-805 (1996).
36. G. Beni and P. M. Platzman, “Temperature and Polarization Dependence of Extended X-Ray Absorption Fine-Structure Spectra,” *Phys. Rev. B*, **14** [4] 1514-1518 (1976).
37. A. Yoshuasa, K. Nakajima, K. Murai, and M. Okube, “Anharmonic effective pair potentials in CaTiO₃, SrTiO₃ and CaGeO₃ perovskite,” *J. Synch. Rad.*, **8**, 940-942 (2001).
38. C. H. Booth, F. Bridges, G. H. Kwei, J. M. Lawrence, A. L. Cornelius, and J. J. Neumeier, “Lattice effects in La_{1-x}Ca_xMnO₃ (x=0->1): Relationships between distortions, charge distribution, and magnetism,” *Phys. Rev. B*, **57**, 10440-10454 (1998).
39. E. A. Stern, “Number of relevant independent points in X-ray absorption fine-structure spectra,” *Phys. Rev. B*, **48** [13] 9825-9827 (1993).
40. W. C. Hamilton, “Significance Tests on the Crystallographic R-Factor,” *Acta Cryst.*, **18**, 502-510 (1965).

“Remarkable Strontium B-Site Occupancy in Ferroelectric Pb(Zr_{1-x}Ti_x)O₃ Solid Solutions Doped with Cryolite-Type Strontium Niobate”

April 26, 2007

41. J. Freund, “On the Determination of Interatomic Potential Anharmonicities from EXAFS Measurements,” *Phys. Letters A*, **157**, 256-260 (1991).
42. L. Downward, C. H. Booth, W. W. Lukens, F. Bridges, “A variation of the F-test for determining statistical relevance for particular parameters in EXAFS analysis,” pp. 129-131 in *AIP Conference Proceedings of the X-Ray Absorption Fine Structure – XAFS13, 13th International Conference*; Stanford, CA, July 9-14, 2006; Vol. 882. American Institute of Physics, 2007.

VII. Figure Captions

Figure 1: Ideal perovskite-type ABO_3 structure of SrTiO_3 (*STO*). The red spheres at the corners of the cube represent Sr^{2+} ions on *A*-sites, the white sphere at the center represents Ti^{4+} ions on *B*-sites, and the blue spheres represent oxygen. Sr^{2+} ions on the *A*-site are surrounded by the faces of $[\text{TiO}_{6/2}]^{2-}$ octahedra and therefore possess 12 immediate oxygen neighbors (so-called $\text{Sr}(\text{A})\text{-O}$ neighbors). The coordination number of Sr^{2+} in SrTiO_3 is hence $CN_{\text{Sr}}=12$.

Figure 2: Representative XRD pattern (black line) and Rietveld simulation (magenta line) of *PZT:SNO-1* ($\text{Pb}(\text{Zr}_{0.53-0.52}\text{Ti}_{0.47-0.48})\text{O}_3$ doped with ~ 0.5 mol-% of *SNO-1* = $\text{Sr}_4(\text{Sr}_{5/3}\text{Nb}_{7/3})\text{O}_{11.5}\text{V}_{0.5}$). The orange line indicates the balance curve of $\text{XRD intensity}_{\text{measured}}$ (black line) minus $\text{XRD intensity}_{\text{calculated}}$ (magenta line). The expected splitting of XRD reflections according to rhombohedral crystal distortion (Bragg reflections indicated by green squares) and tetragonal crystal distortion (Bragg reflections indicated by blue triangles) in the ferroelectric state of *PZT* near the morphotropic phase boundary is clearly resolved.

Figure 3a: Schematic of the cryolite-type unit cell of $\text{Sr}_8(\text{Sr}_{10/3}\text{Nb}_{14/3})\text{O}_{23}\text{V}_{0.1}$ (that is, two unit cells of *SNO-1* = $\text{Sr}_4(\text{Sr}_{5/3}\text{Nb}_{7/3})\text{O}_{11.5}\text{V}_{0.5}$). The octahedral *B*-sites are predominantly occupied by Sr^{2+} ions (yellow spheres) and Nb^{5+} ions (white spheres) in alternating sequence. The blue spheres represent oxygen and V_O represents an oxygen vacancy. It is apparent that Sr^{2+} ions residing on *B*-sites (yellow spheres) possess coordination number $CN_{\text{Sr}}=6$.

Figure 3b: Portion of the upper right region of the unit cell displayed in Figure 3a, indicating the close relationship of the cryolite-type structure shown in Figure 3a with the perovskite-type ABO_3 structure shown in Figure 1. The red spheres represent Sr^{2+} ions on *A*-sites, the yellow

“Remarkable Strontium *B*-Site Occupancy in Ferroelectric Pb(Zr_{1-x}Ti_x)O₃ Solid Solutions Doped with Cryolite-Type Strontium Niobate”

April 26, 2007

spheres represent Sr²⁺ ions on *B*-sites, the white spheres represent Nb⁵⁺ ions on *B*-sites, and the blue spheres represent oxygen. Please note that the octahedral *B*-sites are occupied by Sr²⁺ ions (yellow spheres) and Nb⁵⁺ ions (white spheres) in alternating sequence. It is apparent that Sr²⁺ ions residing on *A*-sites (red spheres) possess coordination number $CN_{\text{Sr}}=12$.

Figure 4: Representative XRD pattern (black line) and Rietveld simulation (magenta line) of oxygen deficient cryolite-type dopant $\text{SNO-1} = \text{Sr}_4(\text{Sr}_{5/3}\text{Nb}_{7/3})\text{O}_{11.5}\text{V}_{0.0.5}$. The orange line indicates the balance curve of XRD intensity_{measured} (black line) minus XRD intensity_{calculated} (magenta line). The positions of expected Bragg reflections for the cryolite-type structure are indicated by blue triangles.

Figure 5: EXAFS Sr *K*-edge data acquired for $\text{PZT:SNO-1} = (\text{PZT})_{0.995}(\text{SNO-1})_{0.005}(\text{PbO})_{0.01}$ in fluorescence mode for 1 scan (data acquisition time: ~30 min) and 17 scans (data acquisition time: ~7.5 h) as an example of the data quality. The EXAFS Sr *K*-edge data quality of the model compounds was much higher.

Figure 6: Plot of Fourier transforms (FT) of $k^2\chi(k)$ vs. r of EXAFS data for SrTiO₃ (*STO*), Sr₄(Sr_{5/3}Nb_{7/3})O_{11.5}V_{0.0.5} (*SNO-1*), Sr₄(Sr_{4/3}Nb_{8/3})O₁₂ (*SNO-2*), and (PZT)_{0.995}(SNO-1)_{0.005}(PbO)_{0.01} (*PZT:SNO-1*).

Figure 7: Plot of Fourier transform (FT) of $k^2\chi(k)$ vs. r for *PZT:SNO* and corresponding data fits. It is evident that the fit (dotted line) in which Sr²⁺ ions are constrained onto the Pb²⁺ (*A*)-site does not reproduce the data peak (continuous line) at $r \approx 3.3 \text{ \AA}$, while the fit (dashed line)

“Remarkable Strontium *B*-Site Occupancy in Ferroelectric Pb(Zr_{1-x}Ti_x)O₃ Solid Solutions Doped with Cryolite-Type Strontium Niobate”

April 26, 2007

that allows 10 ± 3 % of Sr²⁺ ions on the Zr⁴⁺, Ti⁴⁺ (*B*)-site reproduces the data peak at $r \approx 3.3$ Å very well. Other peaks at higher *r*-values are also better reproduced by the latter fit. The Sr²⁺ *B*-site fraction of 10 ± 3 % is well reproduced at the different EXAFS measurement temperatures.

VIII. Tables

Table 1: Fit Results for EXAFS Analysis of *PZT:SNO-1* Samples.^a

	$f_{\text{B}}(\text{Sr})=0^{\text{b}}$				$f_{\text{B}}(\text{Sr})$ varying ^b		
	$R_{\text{diff}}^{\text{c}}$	$\sigma^2 [\text{\AA}^2]^{\text{d}}$	$R [\text{\AA}]^{\text{e}}$	N^{f}	$\sigma^2 [\text{\AA}^2]^{\text{d}}$	$R [\text{\AA}]^{\text{c}}$	N^{f}
Sr(A)-O	2.559	0.008(6)	2.6(1)	4.0	0.005(3)	2.63(2)	3.6
Sr(A)-O	2.892	0.010	2.76(3)	4.0	0.00654	2.77(2)	3.6
Sr(A)-O	3.273	0.012	3.35(7)	4.0	0.00826	3.41(6)	3.6
Sr(A)-Zr	3.418	0.007(1)	3.27(2)	4.0	0.009(1)	3.26(1)	3.6
Sr(A)-Ti	3.418	0.01042	3.35(2)	4.0	0.01284	3.39(3)	3.6
Sr(A)-Pb	4.046	0.022(9)	4.12(4)	6.0	0.013(4)	4.12(4)	5.4
Sr(A)-Pb	5.722	0.01(10)	6(1)	12.0	0.01(6)	5.92(5)	10.8
Sr(B)-O	1.845	-	-	-	0.00160	1.73(8)	0.1
Sr(B)-O	2.046	-	-	-	0.00250	1.96(3)	0.5
Sr(B)-O	2.295	-	-	-	0.00360	2.19(8)	0.1
Sr(B)-Pb	3.418	-	-	-	0.0005(8)	3.37(1)	0.8
Sr(B)-Zr	4.046	-	-	-	0.0000(1)	4.10(3)	0.3
Sr(B)-Ti	4.046	-	-	-	0.00000	3.77(4)	0.3
Sr(B)-Zr	5.722	-	-	-	0.004(8)	5.52(8)	0.6
Sr(B)-Ti	5.722	-	-	-	0.00587	5(1)	0.6
ΔE_0^{g}		-8(2)			-1(1)		
$f_{\text{B}}(\text{Sr})^{\text{b}}$		0.0			0.10(3)		
dof^{h}		28.4			16.4		
$R [\%]^{\text{j}}$		30.2			15.8		

Footnotes for Table 1:

- ^a: The EXAFS data was measured at a temperature of 20 K. The fit range was 1.20-6.00 Å. The k^2 -weighted data was Fourier transformed between 2.50-15.00 Å⁻¹ and Gaussian narrowed by 0.30 Å⁻¹. The overall scale factor was fixed to $S_0^2=1.0$ for these fits. The second Sr(A)-O pair σ was constrained to be 0.01 Å greater than the first, as was the third Sr(A)-O pair σ constrained to the second. The Sr(B)-O pairs were similarly constrained. The Sr-Ti pair-distance distribution variance values σ^2 were constrained to $(\mu_{\text{Sr-Zr}}/\mu_{\text{Sr-Ti}})\sigma_{\text{Sr-Zr}}^2$ at the same or similar distance, where μ_X is the reduced mass of the *X* scattering pair. Reported errors shown in parenthesis were determined by a Monte-Carlo method and do not reflect systematic errors (see Ref. 28).
- ^b: Fraction of Sr²⁺ cations on the nominal *B*-sites.
- ^c: Expected bond length from respective *A*- and *B*-sites determined from diffraction measurements of *PZT* (see Ref. 3).
- ^d: Pair-distance distribution variance.
- ^e: Atomic distance from respective *A*-sites or *B*-sites.
- ^f: Number of neighbors per Sr²⁺ ion (see Ref. 3).
- ^g: ΔE_0 is the overall shift in the value of E_0 chosen for determining the photoelectron wave vector k .
- ^h: Fit degrees of freedom, determined using *Stern's* rule (see Ref. 39) for the number of independent data points.

“Remarkable Strontium *B*-Site Occupancy in Ferroelectric Pb(Zr_{1-x}Ti_x)O₃ Solid Solutions Doped with Cryolite-Type Strontium Niobate”

April 26, 2007

$$j: R[\%] = \frac{\sum_i (\tilde{\chi}_{R,i} - \tilde{F}_{R,i})^2 + (\tilde{\chi}_{I,i} - \tilde{F}_{I,i})^2}{\sum_i \tilde{\chi}_{R,i}^2 + \tilde{\chi}_{I,i}^2}, \text{ where } \tilde{\chi}_R, \tilde{\chi}_I, \tilde{F}_R, \tilde{F}_I \text{ are the real and imaginary}$$

parts of the Fourier transform of $\chi(k)$ and the fit, respectively.

IX. Figures

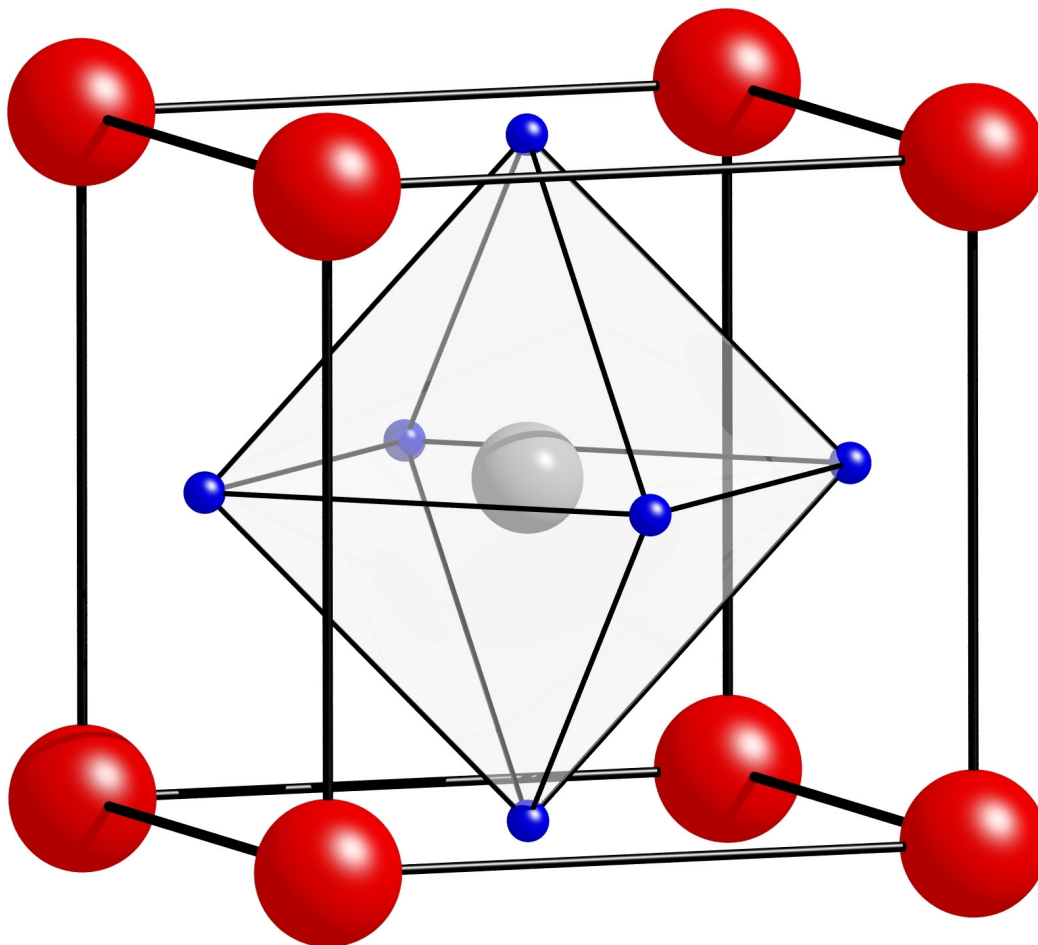


Figure 1

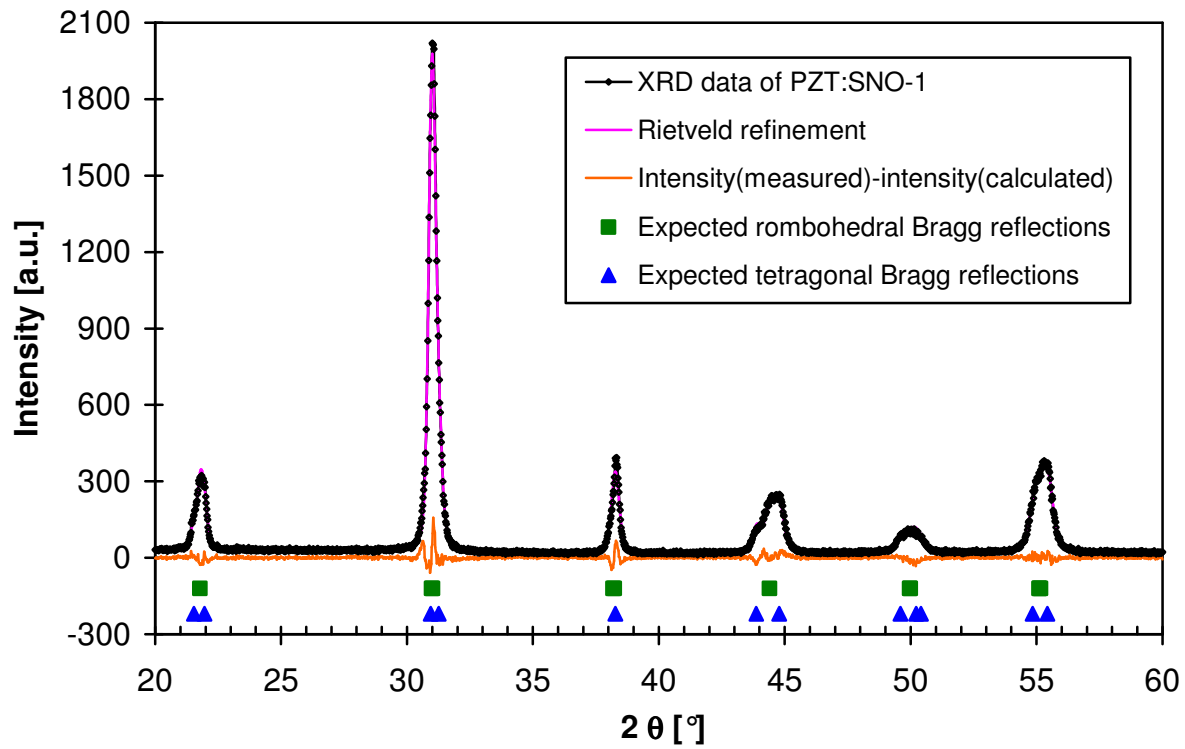


Figure 2

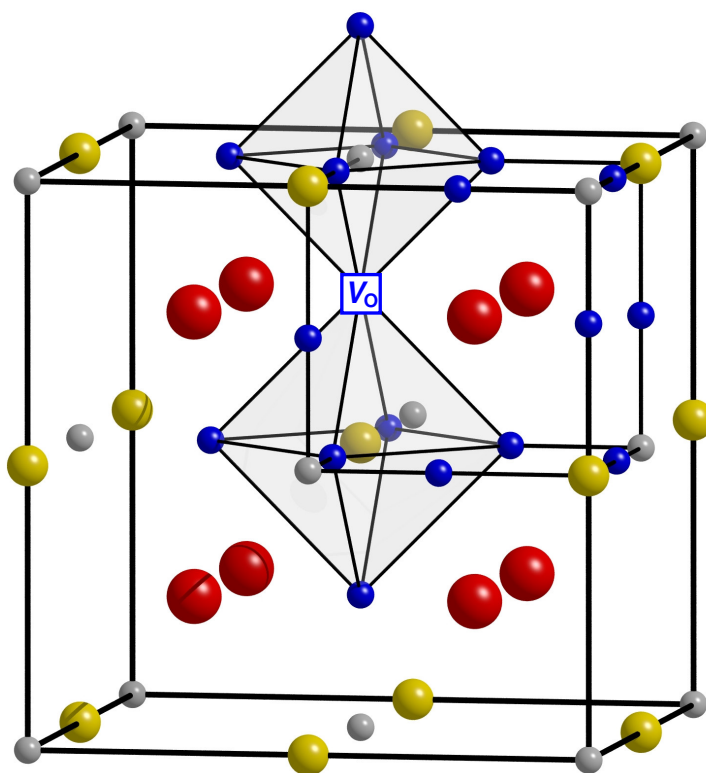


Figure 3a

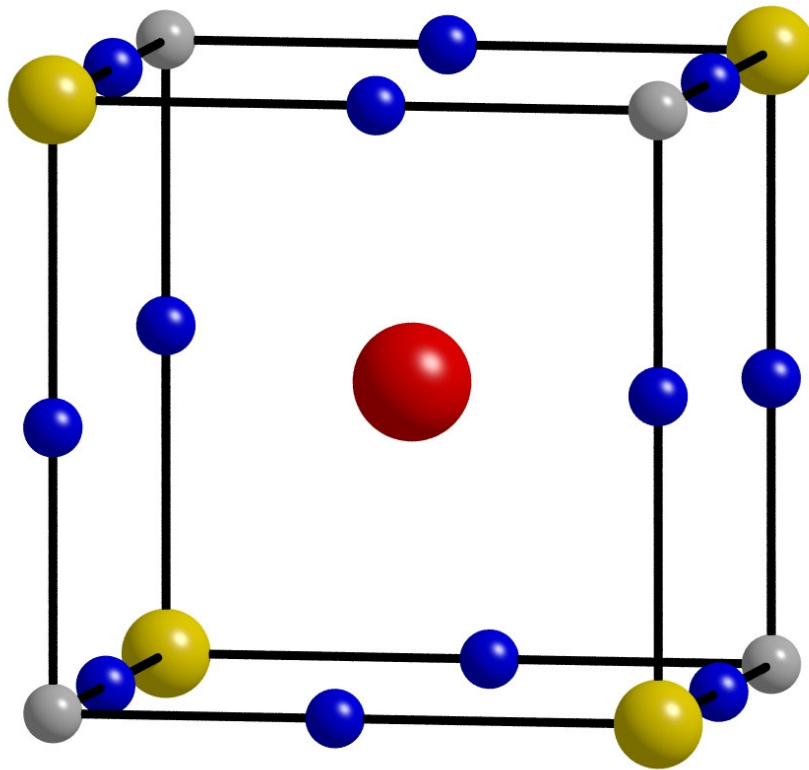


Figure 3b

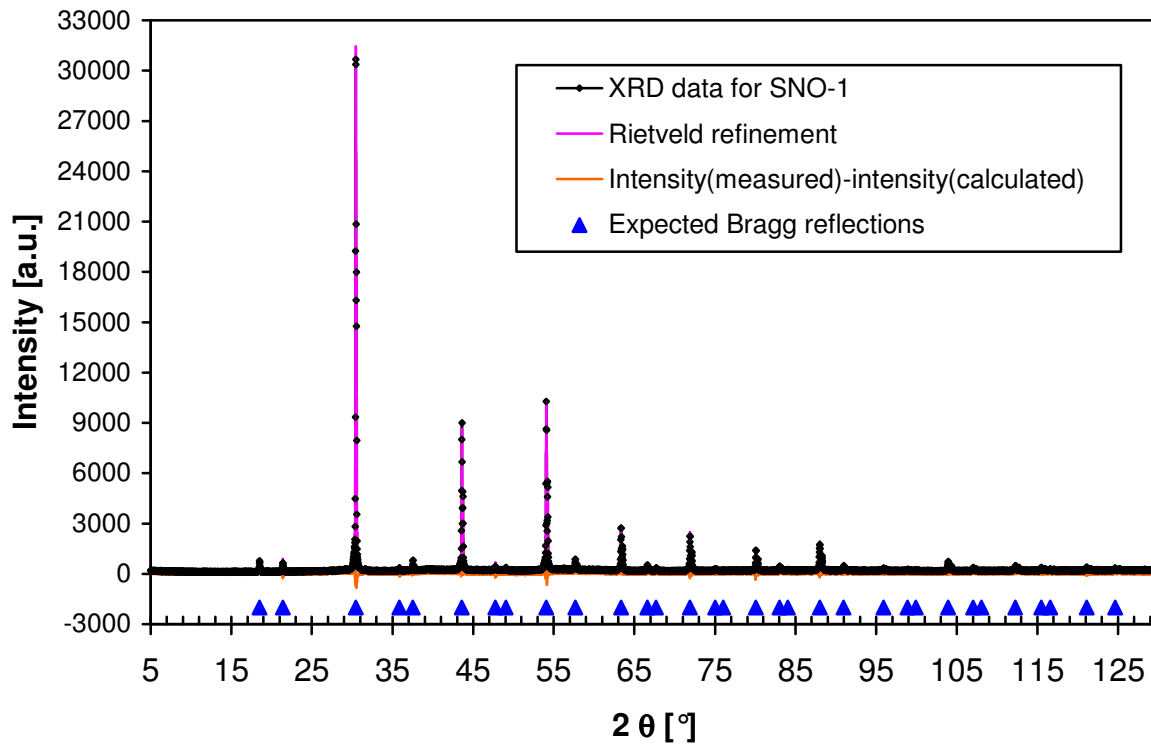


Figure 4

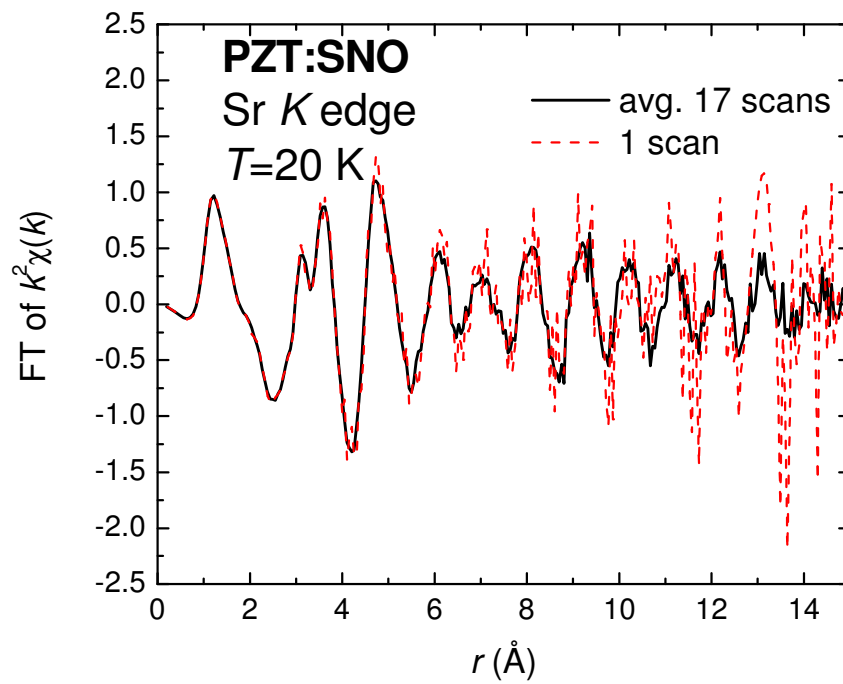


Figure 5

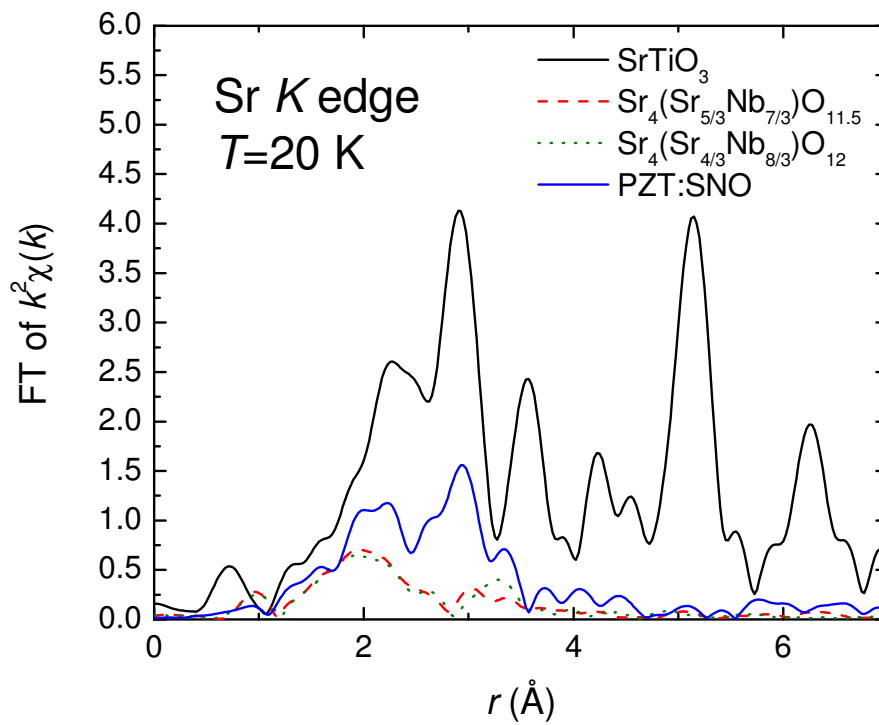


Figure 6

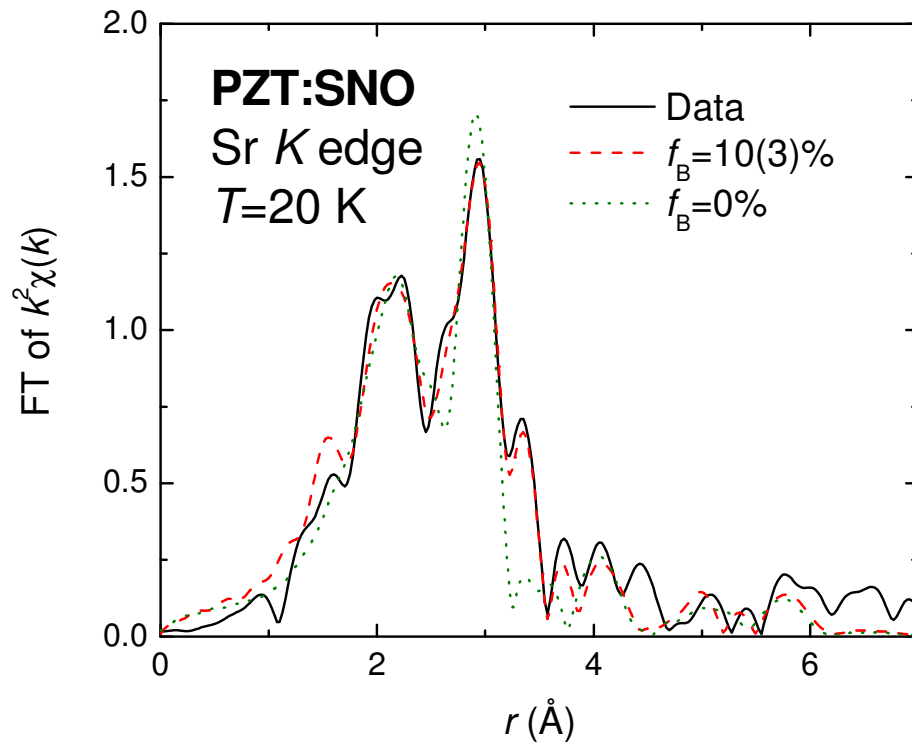


Figure 7